










## Origin of magnetically dead layers in spinel ferrites $M\text{Fe}_2\text{O}_4$ grown on $\text{Al}_2\text{O}_3$ : Effects of postdeposition annealing studied by XMCD

Yosuke Nonaka <sup>1,\*</sup>, Yuki K. Wakabayashi <sup>2</sup>, Goro Shibata <sup>1,3</sup>, Shoya Sakamoto <sup>1,4</sup>, Keisuke Ikeda,<sup>1</sup> Zhendong Chi <sup>1</sup>, Yuxuan Wan <sup>1</sup>, Masahiro Suzuki,<sup>1</sup> Arata Tanaka <sup>5</sup>, Masaaki Tanaka <sup>2,6</sup>, and Atsushi Fujimori <sup>1,7</sup>

<sup>1</sup>Department of Physics, the University of Tokyo, Bunkyo-ku, Tokyo 113-0033, Japan

<sup>2</sup>Department of Electrical Engineering and Information Systems, the University of Tokyo, 7-3-1 Hongo, Bunkyo-ku, Tokyo 113-8656, Japan

<sup>3</sup>Materials Sciences Research Center, Japan Atomic Energy Agency (JAEA), Sayo, Hyogo 679-5148, Japan

<sup>4</sup>The Institute for Solid State Physics, the University of Tokyo, Kashiwa, Chiba 277-8581, Japan

<sup>5</sup>Graduate School of Advanced Science of Matter, Hiroshima University, Higashi-hiroshima, Hiroshima 739-8530, Japan

<sup>6</sup>Center for Spintronics Research Network, Graduate School of Engineering, the University of Tokyo, 7-3-1 Hongo, Bunkyo-ku, Tokyo 113-8656, Japan

<sup>7</sup>Center for Quantum Technology and Department of Physics, National Tsing Hua University, Hsinchu 30013, Taiwan



(Received 5 February 2023; accepted 24 March 2023; published 27 April 2023)

We study the electronic and magnetic states of as-grown and annealed  $M\text{Fe}_2\text{O}_4(111)/\text{Al}_2\text{O}_3(111)$  ( $M = \text{Co}, \text{Ni}$ ) thin films with various thicknesses grown on  $\text{Si}(111)$  substrates with the  $\gamma\text{-Al}_2\text{O}_3(111)$  buffer layers by using x-ray absorption spectroscopy (XAS) and x-ray magnetic circular dichroism (XMCD), to investigate magnetically dead layers in these films. Although the magnetically dead layers in the as-grown samples are formed near the interface with the  $\text{Al}_2\text{O}_3$  buffer layer, we reveal that ferrimagnetic order is partially recovered by postdeposition annealing at 973 K for 48 h in air. By analyzing the line shapes of the XAS and XMCD spectra, we conclude that, in the dead layers, there are a significant number of vacancies at the  $T_d$  sites of the spinel structure, which may be the microscopic origin of the degraded ferrimagnetic order in the  $M\text{Fe}_2\text{O}_4$  thin films.

DOI: [10.1103/PhysRevMaterials.7.044413](https://doi.org/10.1103/PhysRevMaterials.7.044413)

### I. INTRODUCTION

Electronics have achieved great success by controlling the charge degree of freedom of electrons in semiconductors. By adding the spin degree of freedom to the existing electronics, a new field of electronics known as spintronics is being developed. Spintronics devices have several advantages over existing electronic devices, e.g., nonvolatility, low-energy consumption, high speed, infinite endurance [1]. To establish next-generation electronics with semiconductor-based spintronics, injection of spin-polarized carriers into semiconductors should be realized at room temperature by utilizing a magnetic spin injector formed on the semiconductor. The spin filter is a promising technology to inject highly spin-polarized current into semiconductors. Insulating spinel-ferrite thin films are attracting high attention as a promising material for spin filters because they have the down-spin and up-spin conduction bands at different energies [the  $3d-t_{2g}$  band of  $\text{Fe}^{3+}(O_h)$  and the  $3d-e$  band of  $\text{Fe}^{3+}(T_d)$ , as Fig. 1(a)] [2], and their Néel temperatures are much higher than room temperature (790 K for  $\text{CoFe}_2\text{O}_4$  [3–5], and 850 K for  $\text{NiFe}_2\text{O}_4$  [2,6]). However, the experimentally obtained spin-filtering efficiency of ferrite-based tunnel barriers remains considerably lower than the theoretical value of 100% [7–10]. In recent investigation, possible causes for this low

spin-filtering efficiency have been proposed. One is that mid-gap impurity states are induced by structural and/or chemical defects [2,4,11]. For example, in  $\text{CoFe}_2\text{O}_4$ , the presence of  $\text{Co}^{3+}$  degrades the spin filter due to the formation of up-spin states in the middle of the band gap. Another possibility is that layers with degraded magnetic properties are formed in the interfacial region, which is often called magnetically dead layers.<sup>1</sup> They are well known for epitaxial  $\text{Fe}_3\text{O}_4$  thin films grown on  $\text{MgO}$  substrates, and are thought to originate from antiphase boundaries and their antiferromagnetic interdomain exchange interaction [12–16]. In addition, a recent study on epitaxial  $\text{Fe}_3\text{O}_4$  thin films grown on  $\text{MgO}$  substrates revealed that the first  $\text{Fe}_3\text{O}_4$  monolayer lacks  $\text{Fe}^{3+}$  ions at the tetrahedral sites [17], resulting in a loss of the ferrimagnetic order due to missing superexchange paths.

In recent works [18–20], the magnetic properties of  $M\text{Fe}_2\text{O}_4(111)/\text{Al}_2\text{O}_3(111)/\text{Si}(111)$  ( $M = \text{Co}, \text{Ni}$ ) structures [21] were studied using the element-specific probes of x-ray absorption spectroscopy (XAS) and x-ray magnetic circular dichroism (XMCD). The authors revealed that the decrease of the inversion parameter  $y$ , defined by  $=[\text{M}_{1-y}\text{Fe}_y]_{T_d}[\text{Fe}_{2-y}\text{M}_y]_{O_h}\text{O}_4$  is correlated with the formation of magnetically dead layers. The inversion parameter  $y$ , which

<sup>1</sup>We note that dead does not mean completely disordered but partially disordered. Finite spin-filtering efficiencies ( $\sim 4\%$ ) at room temperature have been reported for  $\text{CoFe}_2\text{O}_4$ -based spin-filter devices, where the  $\text{CoFe}_2\text{O}_4$  thickness was 1.5–3 nm [4,11].

\*Present address: Nippon Steel Corporation, Steel Research Laboratories, Japan; nonaka.hb6.yohsuke@jp.nipponsteel.com

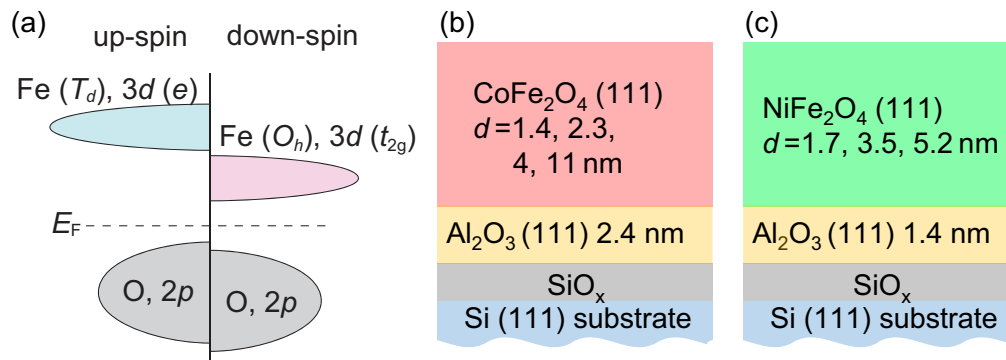


FIG. 1. Schematic description of the electronic structure of  $M\text{Fe}_2\text{O}_4$  ( $M = \text{Co}$  or  $\text{Ni}$ ) and the sample structures. (a) Density of states of the valence-band top and conduction-band bottom for  $M\text{Fe}_2\text{O}_4$ , reproduced from Ref. [19]. (b) Cross-sectional illustration of the  $\text{CoFe}_2\text{O}_4(111)/\text{Al}_2\text{O}_3(111)/\text{Si}(111)$  structure, adapted from Ref. [18]. (c) Cross-sectional illustration of the  $\text{NiFe}_2\text{O}_4(111)/\text{Al}_2\text{O}_3(111)/\text{Si}(111)$  structure, adapted from Ref. [19].

is equal to unity in the ideal inverse spinel, represents the regularity of the cation distribution in the spinel structure. It was found that the reduced thickness of the  $\text{CoFe}_2\text{O}_4$  film leads to a significant reduction in both  $y$  and ferrimagnetic ordered moment. It was also found that  $\text{NiFe}_2\text{O}_4$  has a larger  $y$  ( $=0.79\text{--}0.91$ ) than  $\text{CoFe}_2\text{O}_4$  ( $y = 0.54\text{--}0.75$ ), indicating that Ni has a higher  $O_h$ -site selectivity than Co. Considering that the cation distribution in  $M\text{Fe}_2\text{O}_4$  can be modified by postdeposition annealing [5,22], it is expected that annealing recovers the ferrimagnetic behavior of the interfacial region degraded by the formation of the magnetically dead layers. In the present study, we investigate the electronic and magnetic states of as-grown and annealed  $M\text{Fe}_2\text{O}_4(111)/\text{Al}_2\text{O}_3(111)/\text{Si}(111)$  ( $M = \text{Co}, \text{Ni}$ ) thin films using XAS and XMCD. We reveal that the degraded magnetic properties of the magnetically dead layer can be partially recovered by annealing through the redistribution of the cations. Furthermore, we find that there are a significant number of vacant  $T_d$  sites in the magnetically dead layers, and that such vacancies may degrade the ferrimagnetic order in the  $M\text{Fe}_2\text{O}_4$  thin films.

## II. EXPERIMENTAL METHODS

$\text{CoFe}_2\text{O}_4(111)$  and  $\text{NiFe}_2\text{O}_4(111)$  thin films with various thicknesses were epitaxially grown on  $\text{Al}_2\text{O}_3(111)$  buffer layers formed on  $\text{Si}(111)$  substrates using the pulsed laser deposition (PLD) method. Schematic illustrations of the sample structures are shown in Figs. 1(b) and 1(c). 2.4 nm- and 1.4 nm-thick  $\gamma\text{-Al}_2\text{O}_3(111)$  buffer layers were adopted for  $\text{CoFe}_2\text{O}_4$  and  $\text{NiFe}_2\text{O}_4$  thin films, respectively. The thicknesses of the films were  $d = 1.4, 2.3, 4,$  and  $11$  nm for  $\text{CoFe}_2\text{O}_4$ , and  $d = 1.7, 3.5,$  and  $5.2$  nm for  $\text{NiFe}_2\text{O}_4$ . In order to avoid charging up of the samples during the XAS and XMCD measurements, we used highly phosphorus-doped  $\text{Si}(111)$  substrates with a low electrical resistivity  $2$  m $\Omega$ cm. For the epitaxial growth of the  $\gamma\text{-Al}_2\text{O}_3$  buffer layers on the Si substrates, we used solid-phase reaction of Al and  $\text{SiO}_2$ . More detailed descriptions of sample preparation and characterization are provided in Refs. [18,19]. Some of the  $\text{CoFe}_2\text{O}_4$  and  $\text{NiFe}_2\text{O}_4$  thin films were annealed in order to redistribute the cations in the thin films, aiming at the recovery of the

inversion parameter  $y$ . In order to suppress the oxidation of the Si substrate, the postdeposition annealing temperature was set to 973 K because the oxidation rate of Si rapidly increases particularly above 1073 K [23]. The films were annealed at 973 K for 48 h in air. Since higher inversion parameters of  $\text{CoFe}_2\text{O}_4$  have been reported in slowly cooled bulk crystals than in rapidly quenched ones [5], we set a slow cooling rate of 1 K/min down to 673 K and then the samples were naturally cooled down to room temperature.

XMCD measurements were performed at beam line BL-16A of Photon Factory, High Energy Accelerator Research Organization (KEK-PF). A magnetic field of 5 T was applied parallel to the incident x rays. The measurements were done at room temperature ( $\sim 300$  K). The absorption signals were detected in the total-electron-yield (TEY) mode. Since the probing depth in the TEY mode is a few nm [24,25], the XAS and XMCD spectra of a few nm-thick films reflect the electronic and magnetic properties of the entire  $M\text{Fe}_2\text{O}_4$  film including the magnetically dead layers near the spinel/ $\text{Al}_2\text{O}_3$  interface. By increasing the film thickness to  $\gtrsim 5$  nm, the spectra more strongly reflect the signals away from the interface. The XMCD signals were collected by switching the photon helicity at every energy point.

In order to analyze the XAS and XMCD spectra quantitatively, we performed configuration-interaction (CI) cluster-model calculation [26]. The model is a good approximation for localized electron systems such as the insulating spinel ferrites. In the present calculation, we used an XTLS version 8.5 program [27]. In choosing parameter values for the calculation, we adopted the following empirical rules: (i) The ratio between the on-site Coulomb energy between  $3d$  electrons  $U_{dd}$  and the attractive  $2p$  core hole  $3d$  electron Coulomb energy  $U_{dc}$  was fixed to  $U_{dc}/U_{dd} \sim 1.3$  [28,29]. (ii) The ratio between Slater-Koster parameters ( $pd\sigma$ ) and ( $pd\pi$ ) was fixed to  $(pd\sigma)/(pd\pi) = -2.17$  [30]. The hybridization strength between O  $2p$  orbitals  $T_{pp}$  was fixed to 0.7 eV for the  $O_h$  site and 0 eV for the  $T_d$  site [27,28]. The Slater integrals were set to be 80% of the Hartree-Fock values. Thus, the crystal-field splitting  $10Dq$ , the charge-transfer energy  $\Delta$ ,  $U_{dd}$ , and ( $pd\sigma$ ) were treated as adjustable parameters. As for the Fe cations, the parameters were adjusted to reproduce all the measured Fe  $L_{2,3}$ -edge spectra by the weighted sum of the calculated

TABLE I. Parameter values for the CI cluster-model calculations used in the present study in units of eV. Parameters for  $\text{Fe}^{2+}(O_h)$  were adopted from Ref. [19].

	$\Delta$	$10Dq$	$(pd\sigma)$	$U_{dd}$
$\text{Fe}^{3+}(O_h)$	3.0	0.8	1.5	7.0
$\text{Fe}^{3+}(T_d)$	2.5	-0.5	1.8	6.0
$\text{Fe}^{2+}(O_h)$	6.5	0.9	1.4	6.0

spectra for the  $\text{Fe}^{2+}(O_h)$ ,  $\text{Fe}^{3+}(T_d)$ , and  $\text{Fe}^{3+}(O_h)$  ions. Here, parameters for  $\text{Fe}^{2+}(O_h)$  were adopted from the previous report on  $\text{NiFe}_2\text{O}_4$  [19]. The adjusted parameter values are listed in Table I. As in our previous works [18,19], we fitted the weighted sum of the calculated XAS and XMCD spectra for the  $\text{Fe}^{2+}(O_h)$ ,  $\text{Fe}^{3+}(T_d)$ , and  $\text{Fe}^{3+}(O_h)$  ions to the experimental ones. From this analysis, we obtained the relative amount of the three Fe components and thereby the inversion parameter  $y$ .

### III. RESULTS AND DISCUSSION

#### A. $\text{CoFe}_2\text{O}_4$ thin films

Figure 2 shows the Fe  $L_{2,3}$ -edge XAS ( $\mu^+ + \mu^-$ ) and XMCD ( $\mu^+ - \mu^-$ ) spectra of the  $\text{CoFe}_2\text{O}_4$  thin films with various thicknesses. Here,  $\mu^+$  ( $\mu^-$ ) denote the absorption coefficient for photon helicity parallel (antiparallel) to the majority-spin direction. Figure 2(a) shows that the Fe  $L_{2,3}$ -edge XAS spectral line shapes do not change significantly by postdeposition annealing. In contrast, as shown in Figs. 2(b), the Fe  $L_{2,3}$ -edge XMCD intensities of the annealed samples dramatically increase compared to the as-grown ones, particularly in thinner films ( $d = 1.4$  and  $2.3$  nm). The increase of the XMCD intensities clearly demonstrates that the postdeposition annealing recovers the ferrimagnetic order in the magnetically dead layer of the as-grown films. The  $L_3$ -edge XMCD spectra show characteristic three peaks denoted by **a**, **b**, and **c**. It is well established that the three peaks **a**, **b**, and **c** originate from the  $\text{Fe}^{2+}(O_h)$ ,  $\text{Fe}^{3+}(T_d)$ , and  $\text{Fe}^{3+}(O_h)$  ionic states, respectively [6,9,31,32]. Therefore, one can discuss the Fe-ion distribution in spinel ferrites by estimating the intensities of these XMCD peaks. The spins of the  $\text{Fe}^{3+}(T_d)$  ions are antiferromagnetically coupled with those at the  $O_h$  sites, resulting in the opposite signs between peak **b** and peaks **a** or **c**. Due to these distinct peak features, XMCD spectra are more sensitive to the cation distribution in spinel ferrites than XAS [9,31,32]. Figures 2(c) and 2(d) show comparison of the Fe  $L_3$ -edge XMCD spectral line shapes of the as-grown and annealed  $\text{CoFe}_2\text{O}_4$  films. The spectra have been normalized to the height of peak **c** to compare the spectral line shapes because the  $L_{2,3}$ -edge XMCD intensities decrease with the reduction of the film thickness due to the magnetically dead layers. Figures 2(b) and 2(c) show that the  $L_{2,3}$ -edge XMCD intensity decreases with the reduction of the thickness in the as-grown  $\text{CoFe}_2\text{O}_4$  films and that the XMCD intensity at peak **b** decreases faster than peaks **a** and **c** as previously reported [18]. This indicates the reduction of the  $\text{Fe}^{3+}(T_d)$  component of XMCD in magnetically dead layers near the interface. After postdeposition annealing, as shown in Figs. 2(b) and 2(d),

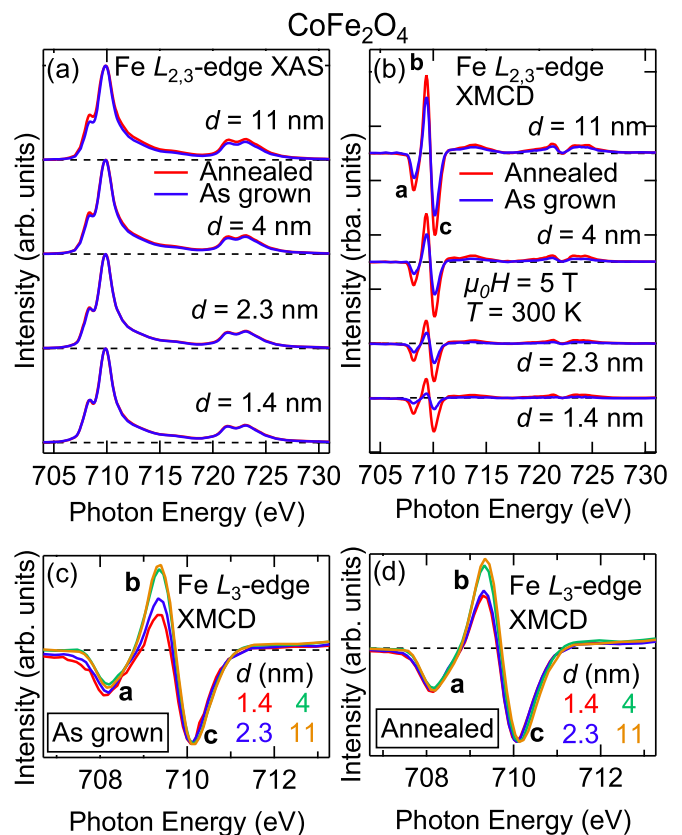


FIG. 2. Fe  $L_{2,3}$ -edge XAS and XMCD spectra of the as-grown and annealed  $\text{CoFe}_2\text{O}_4$  thin films with various thicknesses. (a), (b) Fe  $L_{2,3}$ -edge XAS and XMCD spectra. In (a), a linear and a two-step backgrounds have been subtracted from the raw XAS spectra. The two-step backgrounds are composed of two arctangent functions located at the peak positions of  $L_3$  and  $L_2$  white lines. The height of the  $L_3$  and  $L_2$  steps are set to  $\frac{2}{3}$  and  $\frac{1}{3}$  of the average height around 740 eV, respectively. (c), (d) Magnified views of the Fe  $L_3$ -edge XMCD spectra normalized to the height of peak **c**. The XMCD intensities decrease with decreasing thickness in the as-grown films [(b) and (c)], especially at peak **b**, reflecting the magnetically dead layers near the interface. Both the entire XMCD intensities and the relative intensity at peak **b** are partially recovered by postdeposition annealing particularly in thinner films [(b) and (d)].

both the entire XMCD intensities and the intensity at peak **b** are recovered simultaneously particularly in thinner films. This suggests that the Fe ions are redistributed and that ferrimagnetic order is simultaneously recovered near the interface by annealing.

To clarify the correlation between the cation redistribution and the recovery of the ferrimagnetic order, quantitative spectral line-shape analyses are necessary. We, therefore, performed CI cluster-model calculation to reproduce the experimental XAS and XMCD spectra by the weighted sum of calculated  $\text{Fe}^{2+}(O_h)$ ,  $\text{Fe}^{3+}(T_d)$ , and  $\text{Fe}^{3+}(O_h)$  spectra using the parameters listed in Table I. Figure 3 shows comparison between the experimental and calculated XAS and XMCD spectra at the Fe  $L_{2,3}$  edge. All the experimental spectra are well reproduced by the calculated spectra. Since the amount of the ion is proportional to the weight for each calculated XAS

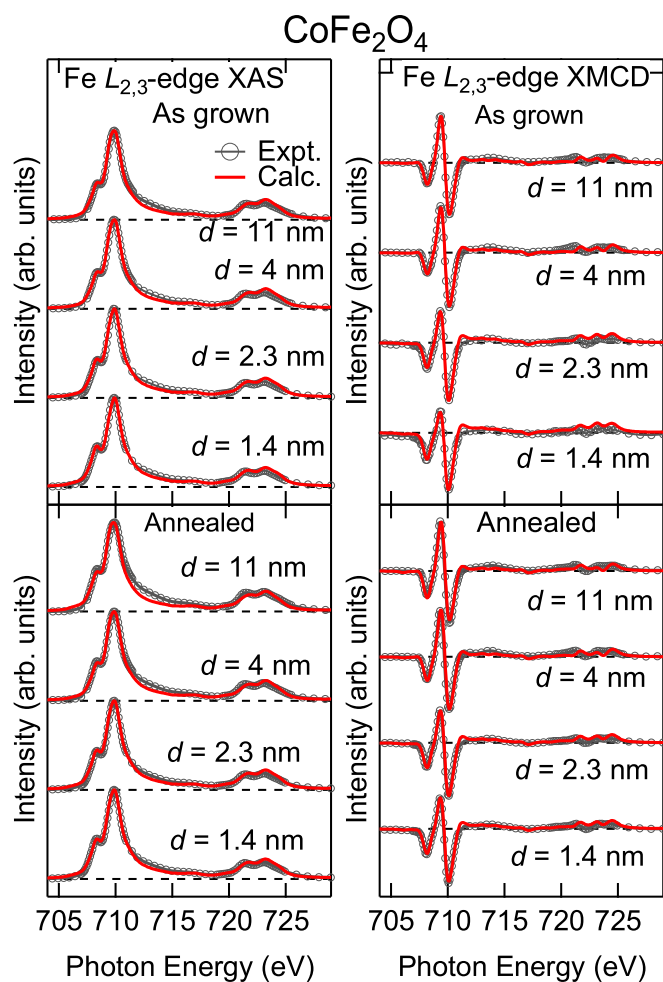


FIG. 3. Comparison between experimental and calculated XAS and XMCD spectra at the Fe  $L_{2,3}$  edge of the as-grown and annealed  $\text{CoFe}_2\text{O}_4$  thin films.

and XMCD spectra, the relative amount can be calculated by the spectral weight ratio. The relative amount deduced from fitting is plotted as functions of film thickness in Fig. 4(a), where the inversion parameter  $y$  is also deduced and plotted. One can see that  $y$  decreases with reducing thickness in the as-grown samples, and that  $y$  increases by the postdeposition annealing. The increase of  $y$  by annealing is more pronounced in the thinner samples, reflecting the redistribution of cations near the interface. Figure 4(b) shows the Fe  $L_3$ -edge XMCD intensities of the as-grown and annealed films as functions of film thickness. The increase ratio of the Fe  $L_3$ -edge XMCD intensity [ $R \equiv \text{XMCD}(\text{annealed})/\text{XMCD}(\text{as grown})$ ] and the increase of the inversion parameter [ $\Delta y \equiv y(\text{annealed}) - y(\text{as grown})$ ] are also shown for comparison. One can see similar thickness dependences between  $R$  and  $\Delta y$ , which suggests that the recovery of the magnetically dead layer is achieved by the redistribution of cations. Based on the above results and the definition of the inversion parameter  $y$  of spinel ferrites ( $[\text{Co}_{1-y}\text{Fe}_y]_{T_d}[\text{Fe}_{2-y}\text{Co}_y]_{O_h}\text{O}_4$ ), one may think that the recovery of the magnetically dead layer by postdeposition annealing is caused by the reduction of the antisites near the interface, that is, the Co ions irregularly occupying the  $T_d$  sites are replaced by Fe ions after annealing. However, one also needs to take into account the cation vacancies at the  $T_d$  sites, as discussed below. Figure 5 shows the Co  $L_{2,3}$ -edge XAS and XMCD spectra for various film thicknesses and the effect of annealing on these spectra. In order to see the changes in the spectral line shapes, we show the Co  $L_3$  edge XMCD spectra normalized to the height of peak **e** in Figs. 5(c) and 5(d). One can see that the positive peak **d** increases by annealing, particularly in the thinner films. As described in the previous report [18], the positive peak at the Co  $L_3$  edge originates from  $\text{Co}^{2+}(T_d)$  ions. Therefore, the increase of peak **d** indicates the increase of the number of ferrimagnetically ordered  $\text{Co}^{2+}(T_d)$  ions near the interface after annealing. The increase of the positive peak components could also explain the slight

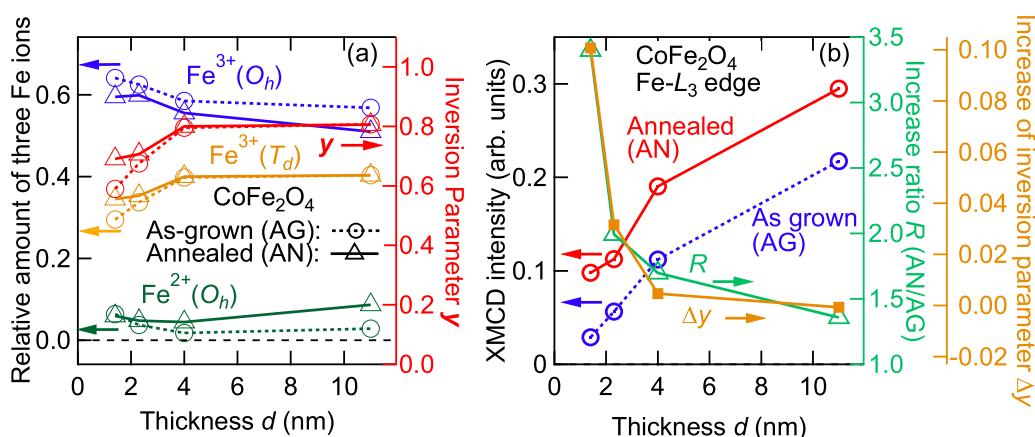


FIG. 4. Thickness dependences of the Fe-ion distribution and the  $L_3$ -edge XMCD intensities for the as-grown and annealed  $\text{CoFe}_2\text{O}_4$  thin films. (a) Relative amount of the  $\text{Fe}^{2+}(O_h)$ ,  $\text{Fe}^{3+}(T_d)$ , and  $\text{Fe}^{3+}(O_h)$  ions as functions of film thickness. The inversion parameter  $y$  is also plotted (right axis). Dashed lines and solid line indicate the as-grown and annealed samples, respectively. (b) Fe  $L_3$ -edge XMCD intensity of the as-grown and annealed films. The increase of  $y$  by annealing ( $\Delta y$ ) and the increase ratio of the XMCD intensity ( $R$ ) are plotted on the right axes. The inversion parameter  $y$  decrease with reducing thickness in the as-grown samples [red dashed line in (a)], and  $y$  increases by annealing [red solid line in (a)].  $\Delta y$  and  $R$  similarly decrease with the film thickness [green and brown lines in (b)], suggesting that the recovery of the magnetically dead layer is achieved by the redistribution of cations.



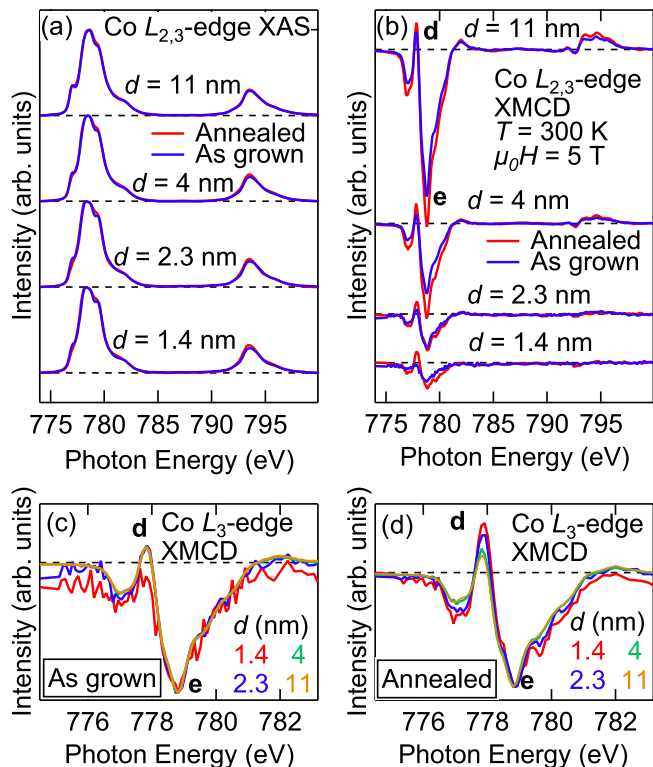


FIG. 5. Co  $L_{2,3}$ -edge XAS and XMCD spectra of the as-grown and annealed  $\text{CoFe}_2\text{O}_4$  thin films with various thicknesses. (a), (b) Co  $L_{2,3}$ -edge XAS and XMCD spectra. (c), (d) Magnified views of Co  $L_3$ -edge XMCD spectra normalized to the height of peak **e**. Since peak **d** originates from  $\text{Co}^{2+}(T_d)$  ions [18], the increase of peak **d** indicates that the number of ferrimagnetically ordered  $\text{Co}^{2+}(T_d)$  ions increase by postdeposition annealing.

increase of the Co  $L_{2,3}$ -edge XMCD intensities by annealing. Surprisingly, not only the number of  $\text{Fe}^{3+}(T_d)$  ions but also that of ferrimagnetically ordered  $\text{Co}^{2+}(T_d)$  ions increase by annealing. These results can be naturally understood if there are a significant number of vacant  $T_d$  sites near the interface of the as-grown  $\text{CoFe}_2\text{O}_4$  thin films and that, after annealing, the vacancies are filled by Fe ions and possibly Co ions, too, diffused from the  $O_h$  sites (for details, see Sec. IV). We note that the inversion parameter  $y$  is defined based on the ideal spinel structure ( $[\text{Co}_{1-y}\text{Fe}_y]_{T_d}[\text{Fe}_{2-y}\text{Co}_y]_{O_h}\text{O}_4$ ) and the vacant sites are not taken into account. The lowering of  $y$  may reflect not only the replacement of the Fe ion by the Co ion but also increase of the vacancies at the  $T_d$  and/or  $O_h$  sites.

Figure 6 shows the Co  $L_3$ -edge XMCD intensities of the as-grown and annealed films as functions of film thickness in the same manner as Fig. 4(b). The increase ratio of the XMCD intensity  $R$  at Co  $L_3$  edge shows a similar thickness dependence as that at the Fe  $L_3$  edge although the values of  $R$  are reduced compared to the case of Fe, particularly in the thinner samples. The reduction of  $R$  is presumably due to the increase of  $\text{Co}^{2+}(T_d)$  ions by annealing. That is, the increase of the XMCD intensities (mainly composed of negative peak components) is offset by the increase of this positive component.

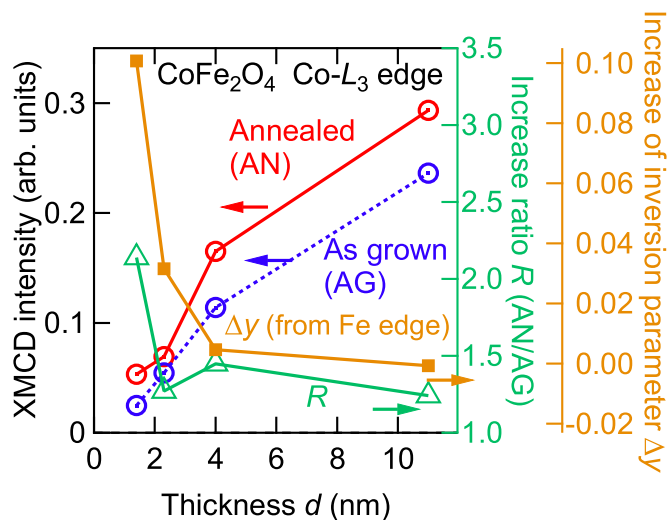


FIG. 6. Thickness dependences of the Co  $L_3$ -edge XMCD intensities for the as-grown and annealed  $\text{CoFe}_2\text{O}_4$  thin films. The increase of  $y$  by annealing ( $\Delta y$ , deduced from Fe  $L_3$ -edge) and the increase ratio of the XMCD intensity ( $R$ ) are plotted on the right axes.

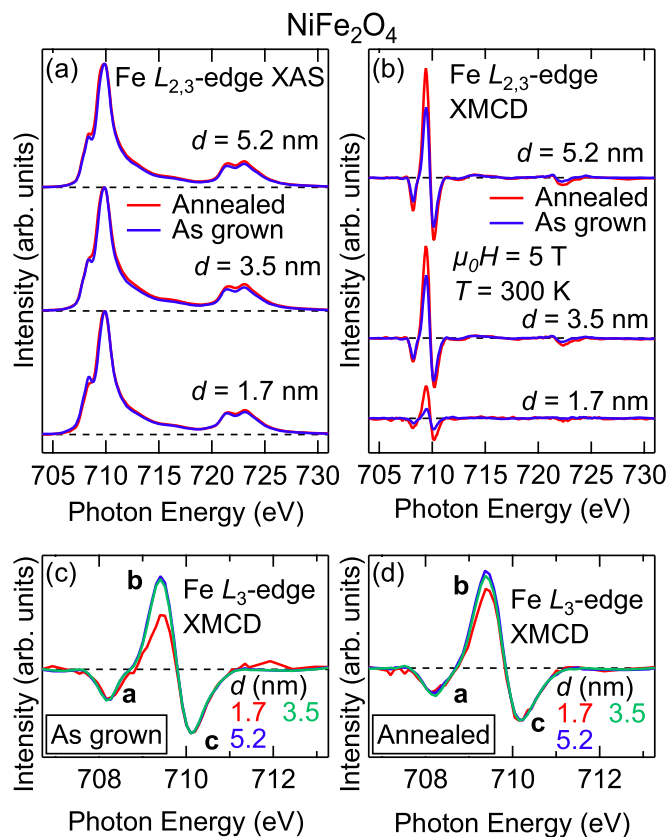


FIG. 7. Fe  $L_{2,3}$ -edge XAS and XMCD spectra of the as-grown and annealed  $\text{NiFe}_2\text{O}_4$  thin films with various thicknesses  $d = 1.7, 3.5,$  and  $5.2$  nm. (a), (b) Fe  $L_{2,3}$ -edge XAS and XMCD spectra. (c), (d) Magnified views of the Fe  $L_3$ -edge XMCD spectra normalized to the height of peak **c**. The changes in the spectra are similar to those of  $\text{CoFe}_2\text{O}_4$  (Fig. 2).

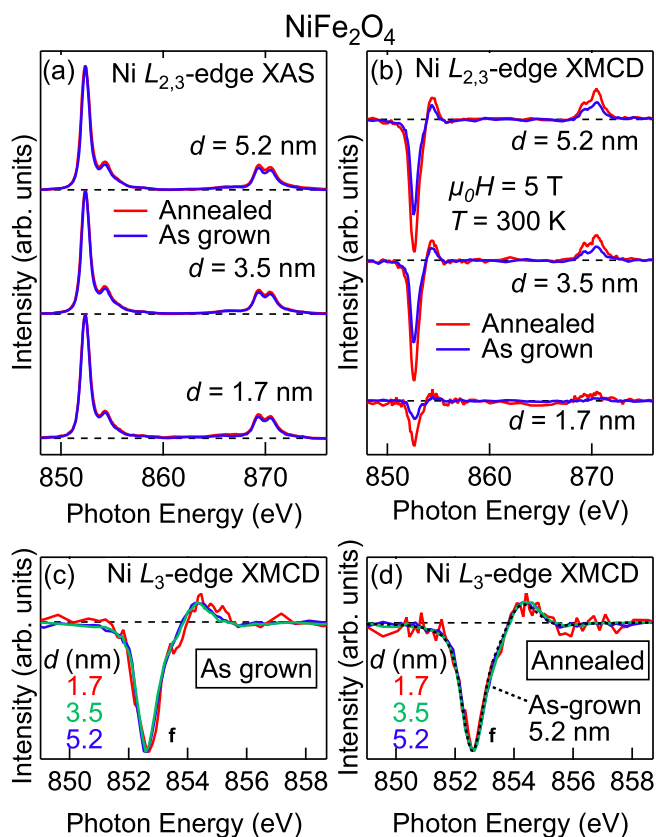


FIG. 8. Ni  $L_{2,3}$ -edge XAS and XMCD spectra of the as-grown and annealed  $\text{NiFe}_2\text{O}_4$  thin films with various thicknesses  $d = 1.7, 3.5,$  and  $5.2$  nm. The spectra of the as-grown films (blue lines) are adopted from Ref. [19]. (a), (b) Ni  $L_{2,3}$ -edge XAS and XMCD spectra. (c), (d) Magnified views of the Ni  $L_3$ -edge XMCD spectra normalized to the height of peak **f** for the as-grown and annealed films. The normalized XMCD spectra of the 5.2-nm-thick as-grown film is also shown by a dashed black curve for comparison. In contrast to the Co  $L_{2,3}$ -edge XMCD spectra shown in Fig. 5, spectral line shapes are not changed by annealing, reflecting the high  $O_h$ -site selectivity of the  $\text{Ni}^{2+}$  ion.

### B. $\text{NiFe}_2\text{O}_4$ thin films

Figure 7 shows the Fe  $L_{2,3}$ -edge XAS and XMCD spectra of the as-grown and annealed  $\text{NiFe}_2\text{O}_4$  thin films with thicknesses  $d = 1.7, 3.5,$  and  $5.2$  nm. Figure 8 shows the Ni  $L_{2,3}$ -edge XAS and XMCD spectra of the  $\text{NiFe}_2\text{O}_4$  films. The XMCD intensity of the 1.7 nm-thick film is extremely low compared to the others, indicating the dominant effect of magnetically dead layers. After annealing, the XMCD intensities increase for all the films. This clearly indicates that the magnetic order in the dead layers was significantly recovered by annealing also in the  $\text{NiFe}_2\text{O}_4$  thin films.

To see the effect of annealing on the cation distribution, we compare the line shapes of normalized XMCD spectra at the Fe and Ni  $L_3$  edges. Figures 7(c) and 7(d) show magnified views of the Fe  $L_3$ -edges XMCD spectra normalized to the height of peak **c**. The spectral line shapes show that the positive peak **b** of the 1.7 nm-thick film significantly increases after annealing, indicating the increase of  $\text{Fe}^{3+}(T_d)$  ions. On the other hand, the Ni-edge XMCD spectral line shapes,

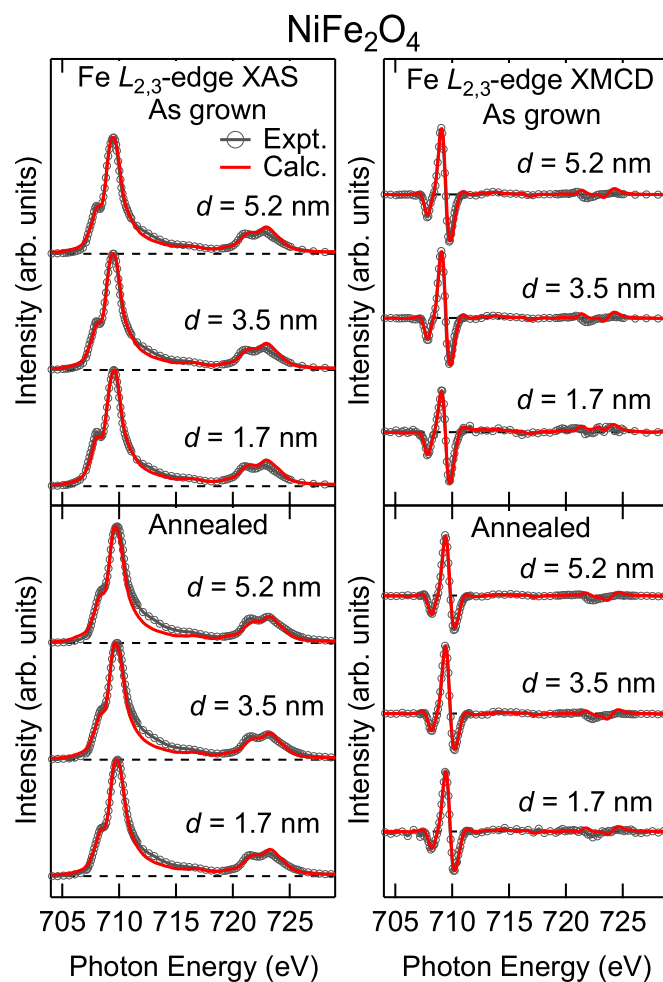


FIG. 9. Comparison between the experimental and calculated Fe  $L_{2,3}$ -edge XAS and XMCD spectra of the as-grown and annealed  $\text{NiFe}_2\text{O}_4$  thin films.

shown in Figs. 8(c) and 8(d), do not show any visible changes depending on the thickness and annealing. The XMCD spectra of the 5.2 nm-thick as-grown film are shown in Fig. 8(d) as a dashed black curve for comparison. One can clearly see that the spectral line shape remains the same after annealing. Because the Ni ion takes only the  $\text{Ni}^{2+}(O_h)$  state, as reported in as-grown films [19], the unchanged spectral line shapes by annealing indicate that the Ni ions did not move to the  $T_d$  sites even after annealing, confirming the high  $O_h$ -site selectivity of the  $\text{Ni}^{2+}$  ion. In order to quantitatively analyze the spectral line shapes of  $\text{NiFe}_2\text{O}_4$ , as in the case of  $\text{CoFe}_2\text{O}_4$ , we fitted the measured Fe  $L_{2,3}$ -edge XAS and XMCD spectra using the weighted sum of the three calculated spectra of  $\text{Fe}^{2+}(O_h)$ ,  $\text{Fe}^{3+}(T_d)$ , and  $\text{Fe}^{3+}(O_h)$  ions. The parameters for the CI cluster model were the same as those for  $\text{CoFe}_2\text{O}_4$  listed in Table I. Figure 9 shows the experimental and calculated Fe  $L_{2,3}$ -edge XAS and XMCD spectra. The experimental spectra are well reproduced by the calculation. Using the weights obtained from the fitting, one can estimate the relative amount of the  $\text{Fe}^{2+}(O_h)$ ,  $\text{Fe}^{3+}(T_d)$ , and  $\text{Fe}^{3+}(O_h)$  ions in the as-grown and annealed  $\text{NiFe}_2\text{O}_4$  thin films as shown in Fig. 10(a). One can see that, for the 1.7 nm-thick film, the ratio of the  $\text{Fe}^{3+}(T_d)$  ions increases with postdeposition annealing, while that of the

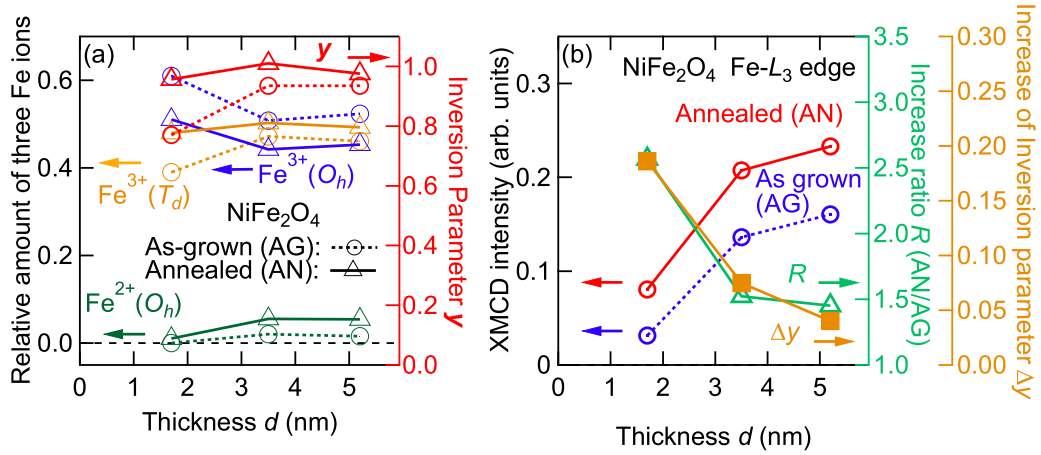


FIG. 10. Thickness dependences of the Fe-ion distribution and the  $L_3$ -edge XMCD intensities for the as-grown and annealed NiFe<sub>2</sub>O<sub>4</sub> thin films. (a) Relative amounts of the Fe<sup>2+</sup>(O<sub>h</sub>), Fe<sup>3+</sup>(T<sub>d</sub>), and Fe<sup>3+</sup>(O<sub>h</sub>) ions in the as-grown and annealed NiFe<sub>2</sub>O<sub>4</sub> thin films as functions of thickness. The inversion parameter  $y$  is also plotted on the right axis. Dashed lines with open circles and solid lines with open triangles indicate as-grown and annealed samples, respectively. (b) Fe  $L_3$ -edge XMCD intensity of the as-grown and annealed films. The increase of  $y$  by annealing ( $\Delta y$ ) and the increase ratio of XMCD intensities ( $R$ ) are plotted on the right axes.

Fe<sup>3+</sup>(O<sub>h</sub>) ions decreases. Thus, the inversion parameter  $y$  of the as-grown 1.7 nm-thick film is low compared to those of the thicker films, consistent with the XMCD result. The low  $y$  value of the 1.7 nm-thick film significantly increases to 0.96 after annealing (red dashed line). This means that NiFe<sub>2</sub>O<sub>4</sub> thin films with almost no antisite defects are achieved after annealing. Figure 10(b) shows the Fe  $L_3$ -edge XMCD intensities of the as-grown and annealed films as functions of film thickness. The increasing ratio of the Fe  $L_3$ -edge XMCD intensity  $R$  and the increase of the inversion parameter  $\Delta y$  are also shown for comparison. Analogously to CoFe<sub>2</sub>O<sub>4</sub> shown in Fig. 4(b), the similar thickness dependences between  $R$  and  $\Delta y$  suggest that the recovery of the magnetically dead layer is achieved by the redistribution of cations.

Figure 11 shows the Ni  $L_3$ -edge XMCD intensities of the as-grown and annealed films as functions of film thickness at the same manner to Fig. 10(b). Unlike the Co  $L_3$ -edge of CoFe<sub>2</sub>O<sub>4</sub> (Fig. 6), the increase ratio  $R$  of the Ni  $L_3$ -edge XMCD intensity is almost the same as that of the Fe  $L_3$ -edge XMCD intensity. This behavior is consistent with our conclusion that the Ni ions do not move to the T<sub>d</sub> sites even after annealing.

The ratio of Fe<sup>3+</sup>(T<sub>d</sub>) to Fe<sup>3+</sup>(O<sub>h</sub>) was about  $\frac{2}{3}$  in the 1.7 nm-thick film before annealing. Considering that the Ni ions are located only at the O<sub>h</sub> sites, one can estimate from this ratio that about  $\frac{1}{3}$  of the T<sub>d</sub> sites should be vacant in the as-grown 1.7 nm-thick film. As we shall discuss below, these vacancies at the T<sub>d</sub> sites should have detrimental effects on the ferrimagnetic order in the spinel structure.

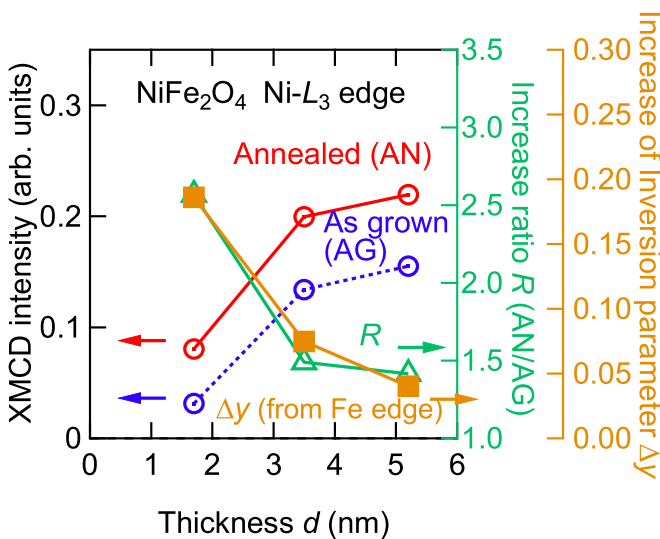


FIG. 11. Thickness dependences of the Ni  $L_3$ -edge XMCD intensities for the as-grown and annealed NiFe<sub>2</sub>O<sub>4</sub> thin films. The increase of  $y$  by annealing ( $\Delta y$ , deduced from Fe  $L_3$ -edge) and the increase ratio of the XMCD intensity ( $R$ ) are plotted on the right axes.

#### IV. DISCUSSION

We discuss the role of the cation vacant sites in the magnetically dead layers. As introduced above, based on the studies on Fe<sub>3</sub>O<sub>4</sub> [12,13,16], it is believed that the magnetically dead

TABLE II. Exchange interaction between transition-metal ions in  $M\text{Fe}_2\text{O}_4$  ( $M = \text{Fe}, \text{Co}$ ) in units of K reproduced from Ref. [33]. Suffixes  $A$  and  $B$  denote the T<sub>d</sub> and O<sub>h</sub> sites, respectively. Note that the listed values include both the superexchange and direct exchange interactions. Positive and negative values correspond to ferromagnetic and antiferromagnetic interactions, respectively.

		$M = \text{Co}$	$M = \text{Ni}$
$J_{AB}$	Fe <sup>3+</sup> -M <sup>2+</sup>	-22.7	-27.4
	Fe <sup>3+</sup> -Fe <sup>3+</sup>	-26	-30.7
$J_{BB}$	M <sup>2+</sup> -M <sup>2+</sup>	46.9	30.0
	Fe <sup>3+</sup> -M <sup>2+</sup>	-18.5	-2.7
	Fe <sup>3+</sup> -Fe <sup>3+</sup>	-7.5	-5.4

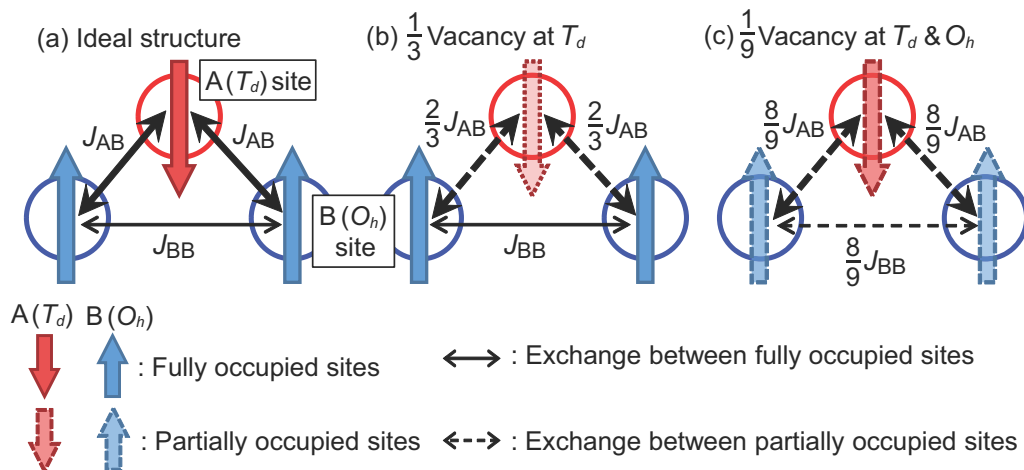


FIG. 12. Schematic pictures of exchange interaction between the  $T_d$ - and  $O_h$ -site ions. The  $T_d$  and  $O_h$  sites are labeled A and B, respectively.

layers in the spinel ferrites are caused by antiphase boundaries. However, as shown above, we find that there are a significant number of vacant  $T_d$  sites near the interface, and the transfer of the cations from the  $O_h$  to  $T_d$  sites caused by annealing significantly recovers the ferrimagnetic order. The antiferromagnetic superexchange interaction between the  $T_d$ -site and  $O_h$ -site cations is the origin of the ferrimagnetic order in the spinel ferrites. Therefore, the lack of superexchange interaction due to the vacancies should significantly suppress the ferrimagnetism of magnetically dead layers. Here, we focus on how the vacant  $T_d$  sites affect the spin structures in the magnetically dead layers. Figure 12(a) shows the exchange interaction between the cations at the  $O_h$  and  $T_d$  sites of the spinel structure. The values of the exchange interaction in  $M\text{Fe}_2\text{O}_4$  ( $M = \text{Co}, \text{Ni}$ ) deduced from magnetization measurements [33], which are denoted as  $J_{AB}$  and  $J_{BB}$  in Fig. 12, are listed in Table II in units of K. We note that suffix A (B) denotes the  $T_d$  ( $O_h$ ) sites, and the ratio between  $M^{2+}(O_h)$ ,  $\text{Fe}^{3+}(T_d)$ , and  $\text{Fe}^{3+}(O_h)$  is 1 : 1 : 1 in an ideal inverse spinel structure. The large negative values of  $J_{AB}$  demonstrate the strong contributions of the  $T_d$  site to the ferrimagnetic order. As for the  $O_h$ - $O_h$  interaction,  $J_{BB}$ , one can see large positive values for  $M^{2+}$ - $M^{2+}$  interaction, and negative ones for  $\text{Fe}^{3+}$ - $\text{Fe}^{3+}$  and  $\text{Fe}^{3+}$ - $M^{2+}$  interactions. On average,  $O_h$ - $O_h$  interactions are weakly ferromagnetic (+0.6 K for  $\text{CoFe}_2\text{O}_4$  and +4.8 K for  $\text{NiFe}_2\text{O}_4$ ).<sup>2</sup> We note that the number of the  $O_h$ - $T_d$  exchange pairs in an ideal spinel structure are 2.3 times larger than that of the  $O_h$ - $O_h$  ones [13]. If  $\frac{1}{3}$  of the  $T_d$  site is vacant as shown in Fig. 12(b),  $J_{AB}$  is weakened to  $\frac{2}{3}$  of the ideal value, degrading the ferrimagnetic order. After annealing, some  $O_h$ -site ions move to  $T_d$  sites. For simplicity, assuming that the vacancies at the  $T_d$  sites are equally redistributed to all the  $T_d$  and  $O_h$  sites, as shown in Fig. 12(c), antiferromagnetic  $J_{AB}$  is recovered to  $\frac{8}{9}$  of ideal value. Since the value and number of exchange interactions of  $J_{AB}$  are larger than that of  $J_{BB}$ , ferrimagnetic

order should be stabilized. Although the actual numbers of the vacancies are still unclear, it can be concluded that vacancies at the  $O_h$  sites still preserve the ferrimagnetic order, whereas vacancies at the  $T_d$  sites significantly degrade the ferrimagnetic order. We should note that the above discussion ignores the effects of charge unbalance caused by the cation vacancies, that is, the effects of cation valence changes and possible oxygen vacancies. We speculate that there are oxygen vacancies [34] and/or that extra  $O_h$  sites [17] near the interface.

## V. CONCLUSION

We have studied the electronic and magnetic states of the as-grown and annealed  $\text{CoFe}_2\text{O}_4(111)$  and  $\text{NiFe}_2\text{O}_4(111)$  thin films with various thicknesses grown on Si substrates with the  $\gamma$ - $\text{Al}_2\text{O}_3$  buffer layers. By analyzing the spectral line shapes using the CI cluster-model calculation, we have estimated the valences and site occupancies of Fe ions. We confirmed through the significant reduction of the XMCD intensities with decreasing film thickness that there are magnetically dead layers near the interface with  $\gamma$ - $\text{Al}_2\text{O}_3$  (the Fe  $L_3$ -edge XMCD intensities of the  $\text{CoFe}_2\text{O}_4$  and  $\text{NiFe}_2\text{O}_4$  films decreased by 87% and 80% from the thickest to the thinnest films, respectively). As reported in the previous works [18,19], the reduction of the inversion parameters was observed in the magnetically dead layers. By annealing the films for 48 h in air to redistribute the cations, the XMCD intensity and inversion parameters significantly increase particularly in the thinner films. Furthermore, from comparison between the results on the as-grown and annealed films, it is suggested that there are a significant number of vacant  $T_d$  sites in the magnetically dead layers. After the postdeposition annealing, the vacancies at the  $T_d$  sites are partially occupied by ions diffused from the  $O_h$  sites. Thus, we conclude that vacant  $T_d$  sites play an important role in the formation of the magnetically dead layers in spinel ferrites.

## ACKNOWLEDGMENTS

We would like to thank Ryosho Nakane for valuable advice and enlightening discussion throughout the

<sup>2</sup>The number of  $\text{Fe}^{3+}$ - $M^{2+}$  exchange pairs is twice as much as that of  $M^{2+}$ - $M^{2+}$  and  $\text{Fe}^{3+}$ - $\text{Fe}^{3+}$  exchange pairs. Therefore, the weighted average value is  $\frac{1}{4}(J_{BB}^{M^{2+}-M^{2+}} + 2J_{BB}^{\text{Fe}^{3+}-M^{2+}} + J_{BB}^{\text{Fe}^{3+}-\text{Fe}^{3+}})$ .



present work, Kenta Amemiya and Masako Suzuki-Sakamaki for valuable technical support at KEK-PF BL-16A. This work was supported by KAKENHI grants from JSPS (JP15H02109, JP26289086, JP15K17696, JP19K03741, JP20K14416, JP20H02199, and JP22K03535). The experiment was done under the approval of the Photon Factory Program Advisory Committee (Proposal No. 2016S2-0056). Y.K.W. and Z.C. acknowledge financial sup-

port from Materials Education Program for the Futures leaders in Research, Industry and Technology (MERIT). Y.W. acknowledges financial support from Advanced Leading Graduate Course for Photon Science (ALPS). Y.K.W. also acknowledges support from the JSPS Research Fellowship Program for Young Scientists. A.F. acknowledges the support from the Yushan Fellow Program under the Ministry of Education (MOE) in Taiwan.

- 
- [1] S. A. Wolf, D. D. Awschalom, R. A. Buhrman, J. M. Daughton, S. vonar Molna, M. L. Roukes, A. Y. Chtchelkanova, and D. M. Treger, Spintronics: A spin-based electronics vision for the future, *Science* **294**, 1488 (2001).
- [2] Z. Szotek, W. M. Temmerman, D. Ködderitzsch, A. Svane, L. Petit, and H. Winter, Electronic structures of normal and inverse spinel ferrites from first principles, *Phys. Rev. B* **74**, 174431 (2006).
- [3] Y. Suzuki, R. B. van Dover, E. M. Gyorgy, J. M. Phillips, V. Korenivski, D. J. Werder, C. H. Chen, R. J. Cava, J. J. Krajewski, W. F. Peck Jr., and K. B. Do, Structure and magnetic properties of epitaxial spinel ferrite thin films, *Appl. Phys. Lett.* **68**, 714 (1996).
- [4] A. V. Ramos, M.-J. Guittet, J.-B. Moussy, R. Mattana, C. Deranlot, F. Petroff, and C. Gatel, Room temperature spin filtering in epitaxial cobalt-ferrite tunnel barriers, *Appl. Phys. Lett.* **91**, 122107 (2007).
- [5] G. A. Sawatzky, F. van der Woude, and A. H. Morrish, Cation distributions in octahedral and tetrahedral sites of the ferrimagnetic spinel  $\text{CoFe}_2\text{O}_4$ , *J. Appl. Phys.* **39**, 1204 (1968).
- [6] S. Matzen, J.-B. Moussy, P. Wei, C. Gatel, J. C. Cezar, M. A. Arrio, P. Sainctavit, and J. S. Moodera, Structure, magnetic ordering, and spin filtering efficiency of  $\text{NiFe}_2\text{O}_4$  (111) ultrathin films, *Appl. Phys. Lett.* **104**, 182404 (2014).
- [7] S. Matzen, J. B. Moussy, R. Mattana, K. Bouzehouane, C. Deranlot, and F. Petroff, Nanomagnetism of cobalt ferrite-based spin filters probed by spin-polarized tunneling, *Appl. Phys. Lett.* **101**, 042409 (2012).
- [8] J. S. Moodera, T. S. Santos, and T. Nagahama, The phenomena of spin-filter tunnelling, *J. Phys.: Condens. Matter* **19**, 165202 (2007).
- [9] J.-B. Moussy, From epitaxial growth of ferrite thin films to spin-polarized tunnelling, *J. Phys. D: Appl. Phys.* **46**, 143001 (2013).
- [10] U. Lüders, M. Bibes, K. Bouzehouane, E. Jacquet, J.-P. Contour, S. Fusil, J.-F. Bobo, J. Fontcuberta, A. Barthélémy, and A. Fert, Spin filtering through ferrimagnetic  $\text{NiFe}_2\text{O}_4$  tunnel barriers, *Appl. Phys. Lett.* **88**, 082505 (2006).
- [11] Y. K. Takahashi, S. Kasai, T. Furubayashi, S. Mitani, K. Inomata, and K. Hono, High spin-filter efficiency in a Co ferrite fabricated by a thermal oxidation, *Appl. Phys. Lett.* **96**, 072512 (2010).
- [12] D. T. Margulies, F. T. Parker, F. E. Spada, R. S. Goldman, J. Li, R. Sinclair, and A. E. Berkowitz, Anomalous moment and anisotropy behavior in  $\text{Fe}_3\text{O}_4$  films, *Phys. Rev. B* **53**, 9175 (1996).
- [13] D. T. Margulies, F. T. Parker, M. L. Rudee, F. E. Spada, J. N. Chapman, P. R. Aitchison, and A. E. Berkowitz, Origin of the Anomalous Magnetic Behaviour in Single Crystal  $\text{Fe}_3\text{O}_4$  Films, *Phys. Rev. Lett.* **79**, 5162 (1997).
- [14] F. C. Voigt, T. T. M. Palstra, L. Niesen, O. C. Rogojanu, M. A. James, and T. Hibma, Superparamagnetic behavior of structural domains in epitaxial ultrathin magnetite films, *Phys. Rev. B* **57**, R8107 (1998).
- [15] W. Eerenstein, T. T. M. Palstra, T. Hibma, and S. Celotto, Origin of the increased resistivity in epitaxial  $\text{Fe}_3\text{O}_4$  films, *Phys. Rev. B* **66**, 201101(R) (2002).
- [16] J.-B. Moussy, S. Gota, A. Bataille, M.-J. Guittet, M. Gautier-Soyer, F. Delille, B. Dieny, F. Ott, T. D. Doan, P. Warin, P. Bayle-Guillemaud, C. Gatel, and E. Snoeck, Thickness dependence of anomalous magnetic behavior in epitaxial  $\text{Fe}_3\text{O}_4$ (111) thin films: Effect of density of antiphase boundaries, *Phys. Rev. B* **70**, 174448 (2004).
- [17] C. F. Chang, Z. Hu, S. Klein, X. H. Liu, R. Sutarto, A. Tanaka, J. C. Cezar, N. B. Brookes, H.-J. Lin, H. H. Hsieh, C. T. Chen, A. D. Rata, and L. H. Tjeng, Dynamic Atomic Reconstruction: How  $\text{Fe}_3\text{O}_4$  Thin Films Evade Polar Catastrophe for Epitaxy, *Phys. Rev. X* **6**, 041011 (2016).
- [18] Y. K. Wakabayashi, Y. Nonaka, Y. Takeda, S. Sakamoto, K. Ikeda, Z. Chi, G. Shibata, A. Tanaka, Y. Saitoh, H. Yamagami, M. Tanaka, A. Fujimori, and R. Nakane, Electronic structure and magnetic properties of magnetically dead layers in epitaxial  $\text{CoFe}_2\text{O}_4/\text{Al}_2\text{O}_3/\text{Si}(111)$  films studied by x-ray magnetic circular dichroism, *Phys. Rev. B* **96**, 104410 (2017).
- [19] Y. K. Wakabayashi, Y. Nonaka, Y. Takeda, S. Sakamoto, K. Ikeda, Z. Chi, G. Shibata, A. Tanaka, Y. Saitoh, H. Yamagami, M. Tanaka, A. Fujimori, and R. Nakane, Cation distribution and magnetic properties in ultrathin  $(\text{Ni}_{1-x}\text{Co}_x)\text{Fe}_2\text{O}_4(x = 0 - 1)$  layers on Si(111) studied by soft x-ray magnetic circular dichroism, *Phys. Rev. Mater.* **2**, 104416 (2018).
- [20] Y. Nonaka, Y. K. Wakabayashi, G. Shibata, S. Sakamoto, K. Ikeda, Z. Chi, Y. Wan, M. Suzuki, T. Koide, M. Tanaka, R. Nakane, and A. Fujimori, Reduced magnetocrystalline anisotropy of  $\text{CoFe}_2\text{O}_4$  thin films studied by angle-dependent x-ray magnetic circular dichroism, *AIP Adv.* **11**, 085317 (2021).
- [21] R. Bachelet, P. de Coux, B. Warot-Fonrose, V. Skumryev, G. Niu, B. Vilquin, G. Saint-Girons, and F. Sánchez, Functional spinel oxide heterostructures on silicon, *CrystEngComm* **16**, 10741 (2014).
- [22] G. Hu, J. H. Choi, C. B. Eom, V. G. Harris, and Y. Suzuki, Structural tuning of the magnetic behavior in spinel-structure ferrite thin films, *Phys. Rev. B* **62**, R779 (2000).
- [23] B. E. Deal and A. S. Grove, General Relationship for the Thermal Oxidation of Silicon, *J. Appl. Phys.* **36**, 3770 (1965).
- [24] B. T. Thole, G. van der Laan, J. C. Fuggle, G. A. Sawatzky, R. C. Karnatak, and J.-M. Esteve,  $3d$  x-ray-absorption lines and the  $3d^9 4f^{n+1}$  multiplets of the lanthanides, *Phys. Rev. B* **32**, 5107 (1985).

- [25] B. H. Frazer, B. Gilbert, B. R. Sonderegger, and G. De Stasio, The probing depth of total electron yield in the sub-keV range: TEY-XAS and X-PEEM, *Surf. Sci.* **537**, 161 (2003).
- [26] A. E. Bocquet, T. Mizokawa, T. Saitoh, H. Namatame, and A. Fujimori, Electronic structure of 3d-transition-metal compounds by analysis of the 2p core-level photoemission spectra, *Phys. Rev. B* **46**, 3771 (1992).
- [27] A. Tanaka and T. Jo, Resonant 3d, 3p and 3s photoemission in transition metal oxides predicted at 2p threshold, *J. Phys. Soc. Jpn.* **63**, 2788 (1994).
- [28] J. Chen, D. J. Huang, A. Tanaka, C. F. Chang, S. C. Chung, W. B. Wu, and C. T. Chen, Magnetic circular dichroism in Fe 2p resonant photoemission of magnetite, *Phys. Rev. B* **69**, 085107 (2004).
- [29] S. Hüfner, *Photoelectron Spectroscopy*, 3rd ed., Advanced Texts in Physics (Springer, Berlin, 2003).
- [30] W. A. Harrison, *Electronic Structure and the Properties of Solids*, 3rd ed. (Freeman, San Francisco, 1980).
- [31] S. Matzen, J. B. Moussy, R. Mattana, F. Petroff, C. Gatel, B. Warot-Fonrose, J. C. Cezar, A. Barbier, M. A. Arrio, and P. Sainctavit, Restoration of bulk magnetic properties by strain engineering in epitaxial  $\text{CoFe}_2\text{O}_4$  (001) ultrathin films, *Appl. Phys. Lett.* **99**, 052514 (2011).
- [32] J. Takaobushi, M. Ishikawa, S. Ueda, E. Ikenaga, J.-J. Kim, M. Kobata, Y. Takeda, Y. Saitoh, M. Yabashi, Y. Nishino, D. Miwa, K. Tamasaku, T. Ishikawa, I. Satoh, H. Tanaka, K. Kobayashi, and T. Kawai, Electronic structures of  $\text{Fe}_{3-x}\text{M}_x\text{O}_4$  ( $M = \text{Mn}, \text{Zn}$ ) spinel oxide thin films investigated by x-ray photoemission spectroscopy and x-ray magnetic circular dichroism, *Phys. Rev. B* **76**, 205108 (2007).
- [33] C. M. Srivastava, G. Srinivasan, and N. G. Nanadikar, Exchange constants in spinel ferrites, *Phys. Rev. B* **19**, 499 (1979).
- [34] G. H. Jaffari, A. K. Rumaiz, J. C. Woicik, and S. I. Shah, Influence of oxygen vacancies on the electronic structure and magnetic properties of  $\text{NiFe}_2\text{O}_4$  thin films, *J. Appl. Phys.* **111**, 093906 (2012).